

<https://doi.org/10.1038/s43246-024-00514-3>

Improved interfacial stability of all-solid-state batteries using cation-anion co-doped glass electrolytes

Check for updates

Rajesh Rajagopal^{1,2}, Yuvaraj Subramanian¹, Sung Kang³, Jungjae Park³ & Kwang-Sun Ryu^{1,2}

The electrochemical performance of all-solid-state batteries needs to be improved by addressing the poor stability against the lithium metal anode and the high interfacial resistance at the cathode–solid electrolyte interface. Here, metal halide-doped $\text{Li}_7\text{P}_2\text{S}_8\text{I}$ -type (LPSI) solid electrolytes are synthesized that improve the electrochemical performance of all-solid-state batteries. The solid electrolytes exhibit a higher ionic conductivity value of 7.77 mS cm^{-1} than bare LPSI solid electrolytes of 3.96 mS cm^{-1} , at room temperature. The metal halide-doped LPSI solid electrolyte is also stable against the lithium metal anode, with a calculated critical current density value of 1 mA cm^{-2} . The fabricated all-solid-state battery shows high electrochemical performance with 99.2% specific capacity retention after 250 cycles at a 0.5 C rate. The results of post galvanostatic charge–discharge analysis confirms that the proposed metal halide-doped LPSI solid electrolyte exhibits improved interfacial stability compared to bare LPSI solid electrolytes.

Recently, all-solid-state lithium batteries have been found to be safer and to fulfill future requirements. The key component of an all-solid-state lithium battery is a solid electrolyte, although various types of solid electrolytes—including garnet, phosphides, nitride, halide, sulfides, oxides, perovskite, etc.—have been proposed, and oxide- and sulfide-based solid electrolytes have received particularly significant research attention^{1–3}. The ionic conductivity of this sulfide-based solid electrolyte is relatively comparable to that of the extensively used conventional liquid-based organic electrolyte^{4–6}.

Among the various sulphide-based solid electrolytes, the $\text{Li}_2\text{S-P}_2\text{S}_5$ binary system has attracted substantial attention due to its unique characteristics. Specifically, the $\text{Li}_2\text{S-P}_2\text{S}_5\text{-LiX}$ type argyrodite and glass ceramic exhibit the highest ionic conductivity ($10^{-2} \text{ S cm}^{-1}$) and electrochemical stability (10 V)^{7–9}. The argyrodite-type solid electrolyte has been widely studied for use in the fabrication of all-solid-state batteries due to its high ionic conductivity and compatibility. Halogen-rich argyrodites have recently been shown to attract considerable attention due to their very high ionic conductivity at room temperature. Excess halogen may occupy the sulfur site and decrease the energy barriers^{4,10}. Unfortunately, the preparation of most of these argyrodite-type solid electrolytes requires a high sintering temperature ($\sim 500 \text{ }^\circ\text{C}$), and it is not stable with lithium metal anode. By contrast, $\text{Li}_7\text{P}_2\text{S}_8\text{X}$ -type glass-ceramic solid electrolyte requires a low sintering temperature ($< 200 \text{ }^\circ\text{C}$) and is highly stable with lithium metal anode^{11,12}. Numerous studies have proven that this $\text{Li}_7\text{P}_2\text{S}_8\text{X}$ -type glass-

ceramic solid electrolyte also exhibits high ionic conductivity after the compositional tuning and doping process. For instance, dual halide-based $\text{Li}_7\text{P}_2\text{S}_8\text{XX}'$ and metal-doped $\text{Li}_7\text{P}_2\text{S}_8\text{XX}'$ glass-ceramic solid electrolytes exhibit high ionic conductivity values of more than 7 mS cm^{-1} at room temperature, which is comparable to that of argyrodite type solid electrolyte. The enhanced ionic conductivity is attributed to the formation of LGPS-like phase^{13,14}.

Although the sulfide-based solid electrolyte exhibits high ionic conductivity, which is a prerequisite for a good all-solid-state lithium battery, the direct usage of this electrolyte is not practical in nature. This is because of a few problems that cannot be overlooked. First, the interfacial stability between the solid electrolyte and the electrode material is poor and decomposes substantially during the electrochemical reaction cycles^{15,16}. The solid electrolyte reacts with electrode material during the electrochemical reaction and generates byproducts that increase the interfacial resistance, eventually causing poor cycle stability. This side reaction can be attributed to the thermodynamic incompatibility between the solid electrolyte and the cathode active material¹⁷. This interfacial side reaction may be reduced by applying the coating layer over the surface of cathode materials, or a stable interfacial (electrolyte) is placed between the solid electrolyte layer and the cathode layer. On the other hand, a thick passivation layer is formed at the solid electrolyte-anode (Li) interface. This mainly occurs due to the instability of sulfide-based solid electrolytes against

¹Department of Chemistry, University of Ulsan, Doowang-dong, Nam-gu, Ulsan 44776, Republic of Korea. ²Energy Harvest Storage Research Center (EHSRC), University of Ulsan, Mugeo-dong, Nam-gu, Ulsan 44610, Republic of Korea. ³Research, Institute of Industrial Science & Technology, San Hyoja-dong Pohang 37673, Republic of Korea. e-mail: ryuks@ulsan.ac.kr

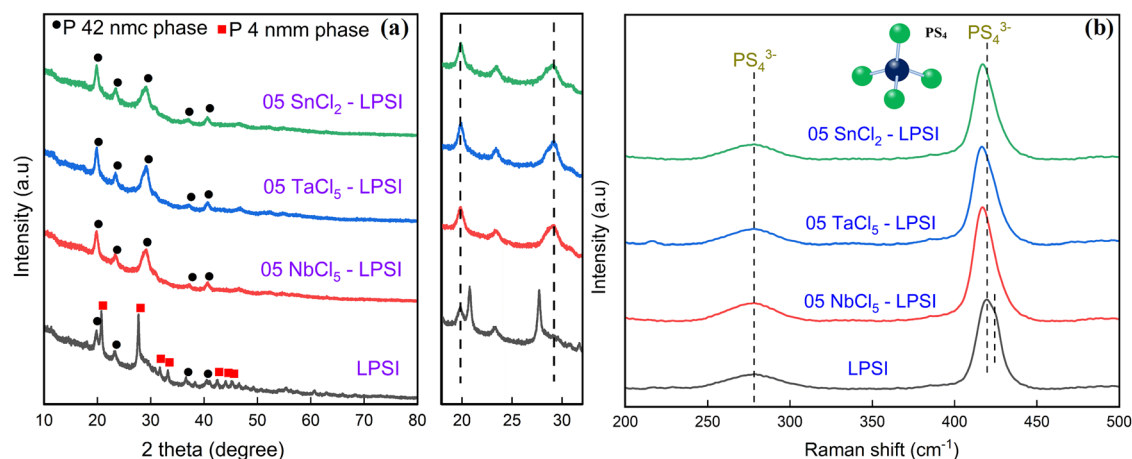


Fig. 1 | Structural analysis of metal halide-doped LPSI solid electrolyte. a XRD pattern and **b** laser Raman spectra of pure and metal halide-doped LPSI solid electrolyte.

lithium metal. Various side products, such as LiX , Li_2S , Li_3P , etc., are formed during the electrochemical reaction and therefore create this passivation layer. These side products lead to the growth of Li dendrites and slow down the Li kinetics, which degrade the performance of the battery. These side reactions may be decreased by enhancing the stability of sulfide-based solid electrolyte against lithium metal anode by changing the composition/doping or introducing a stable intermediate layer between the sulfide-based solid electrolyte and lithium metal anode. $\text{Li}_7\text{P}_2\text{S}_8\text{I}$ solid electrolyte exhibits high stability against lithium metal anode due to the presence of LiI additive¹⁸.

Secondly, sulphide-based solid electrolytes are volatile to moisture and decompose extensively when exposed to air. According to HSAB (Hard Soft Acid Base), in attempts to solve these potential problems, researchers have tried to dope various metals or metal oxides to the sulfide-based solid electrolyte. The addition of metal and metal oxides not only increases the moisture stability according to HSAB theory, but it also improves the interfacial stability by preventing the formation of byproducts with electrode material. In hindsight, there have been very few publications reporting that the addition of metal halide also improves moisture stability and interfacial stability. Very recently, metal halide-based dual-doped argyrodite-type solid electrolyte exhibits improved ionic conductivity and electrochemical performance^{19,20}. To our knowledge, metal halides-doped/mixed $\text{Li}_7\text{P}_2\text{S}_8\text{X}$ and $\text{Li}_7\text{P}_2\text{S}_8\text{XX}'$ solid electrolytes have yet to be reported.

In this work, we have prepared NbCl_5 -, TaCl_5 -, and SnCl_2 -doped $\text{Li}_7\text{P}_2\text{S}_8\text{I}$ solid electrolytes through a high-energy ball milling process. Here we have chosen Nb, Ta, and Sn-based metal halides, because, these elements compatible with $\text{Li}_7\text{P}_2\text{S}_8\text{X}$ -type solid electrolytes and exhibited better electrochemical performances. Further, these metal halides can easily form the Li-metal alloy during the electrochemical reaction; which is more stable with lithium metal anode and will improve the stability against lithium metal anode. The metal halide-doped solid electrolytes was used to fabricate all solid-state batteries, and their electrochemical performance was studied. The fabricated all-solid-state batteries with the proposed architecture exhibit a high specific capacity of 183.3 mAh g^{-1} (0.1 C rate) and superior cyclic stability (98.6% specific capacity retention after 100 cycles) compared to undoped $\text{Li}_7\text{P}_2\text{S}_8\text{I}$ solid electrolyte-based all solid-state lithium batteries.

Results and discussion

Structural and morphological analysis

The X-ray diffraction (XRD) analysis was performed for pure and various metal halide-doped LPSI solid electrolytes, and the corresponding XRD patterns are shown in Fig. 1a. At low-temperature heat treatment, i.e., exactly at 200°C , we have observed peaks at 19.8° , 20.8° , 23.4° , 27.7° , 31.8° , 33.2° , 37.2° , 40.8° , 42.6° , 44.1° , and 45.3° for the LPSI solid electrolyte. The peaks at 20.8° , 27.7° , 31.8° , 33.2° , 42.6° , 44.1° , and 45.3° correspond to P 4 nmm phase ($\text{Li}_4\text{PS}_4\text{I}$ phase), referred to as the low ionic conducting phase,

and the peaks at 19.8° , 23.4° , 37.2° , and 40.8° correspond to P 42 nmc phase, which is referred to as high ionic conducting phase (LGPS like Thio LISICON II phase)^{13,14}. After metal halide doping, the solid electrolytes only exhibit high ionic conducting phase, and the characteristic peaks are identified at 19.8° , 23.4° , 29.1° , 37.2° and 40.8° . From this XRD analysis, it could be seen that the low ionic conducting phase mostly disappeared after metal halide doping. In addition, no peak shift or impurity phases were observed after metal halide doping proving that the metal cations and halide anions were properly immersed in the crystalline structure without any disturbance. Interestingly, increasing the doping concentration resulted in the formation of a low ionic conducting phase rather than peak shift or impurity peaks (Supplementary Fig. S1). Figure 1b shows the laser Raman spectra of various metal halide-doped LPSI solid electrolytes. The prepared LPSI solid electrolyte exhibits the characteristic peak at 419.7 cm^{-1} that corresponds to the stretching vibration of PS_4^{3-} tetrahedron^{21–23}. In addition to the main characteristic peaks, we also observed small PS_4^{3-} tetrahedron main peaks at 278.5 cm^{-1} and 424 cm^{-1} . After metal halide doping, the main characteristic peaks slightly shifted to a lower wavenumber ($\sim 416 \text{ cm}^{-1}$), and the small PS_4^{3-} tetrahedron main peaks disappeared. This peak shift suggests that the local structure was slightly disturbed as a result of the doping of metal cations (Nb^{5+} , Ta^{5+} , and Sn^{2+}) at the P – site. In addition, the peak shift and disappearance of the small PS_4^{3-} tetrahedron main peak is attributed to the presence of thio-LISICON II phase; where the sulfur-to-phosphorous ratio is high. Thus the laser Raman results well matched with our powder X-ray diffraction analysis^{24,25}. Moreover, we did not observe any characteristics corresponding to the M–S structure due to the low doping concentration. We also did not observe any peak shift at $\sim 278 \text{ cm}^{-1}$.

The formation of chemical sites in the prepared solid electrolytes was studied using solid NMR analysis. The ^7Li and ^{31}P NMR in the spectrum of pure and metal halide-doped LPSI solid electrolytes are shown in Fig. 2a and b. In the ^7Li MAS NMR spectra, a narrowed Lorentzian peak that can be observed at 0.37 ppm corresponds to Li_3PS_4 basic structure²⁶. A small peak shift was observed after metal halide doping/mixing, which confirmed that the doped metal cations disturbed local structural bonding and chemical sites in the proposed crystal system. The ^{31}P MAS NMR spectra of LPSI solid electrolyte show two major peaks at 82.1 ppm and 89.5 ppm, which are attributable to PS_4^{3-} corresponding to $\text{Li}_4\text{PS}_4\text{I}$ phase and thio-LISICON phase II, respectively. These two characteristic peaks suggest the presence of P atoms at the 4d-site that belong to the low ionic conducting phase. We also observed two minor peaks at 86.3 ppm and 77 ppm that correspond to $\beta - \text{Li}_3\text{PS}_4$ phase and thio-LISICON phase II, respectively, and the presence of P atoms at the 2b-site, respectively²⁷. Interestingly, the $\beta - \text{Li}_3\text{PS}_4$ phase peak at 86.3 ppm and the low ionic conducting phase peak at 82.1 ppm disappeared after metal halide doping. At the same time, the intensity of the high ionic conducting phase peak (P atoms at the 2b-site) at 77 ppm is increased. In addition, we also observed another characteristic peak ($\text{P}_2\text{S}_6^{4-}$) at 105 ppm in bare LPSI solid

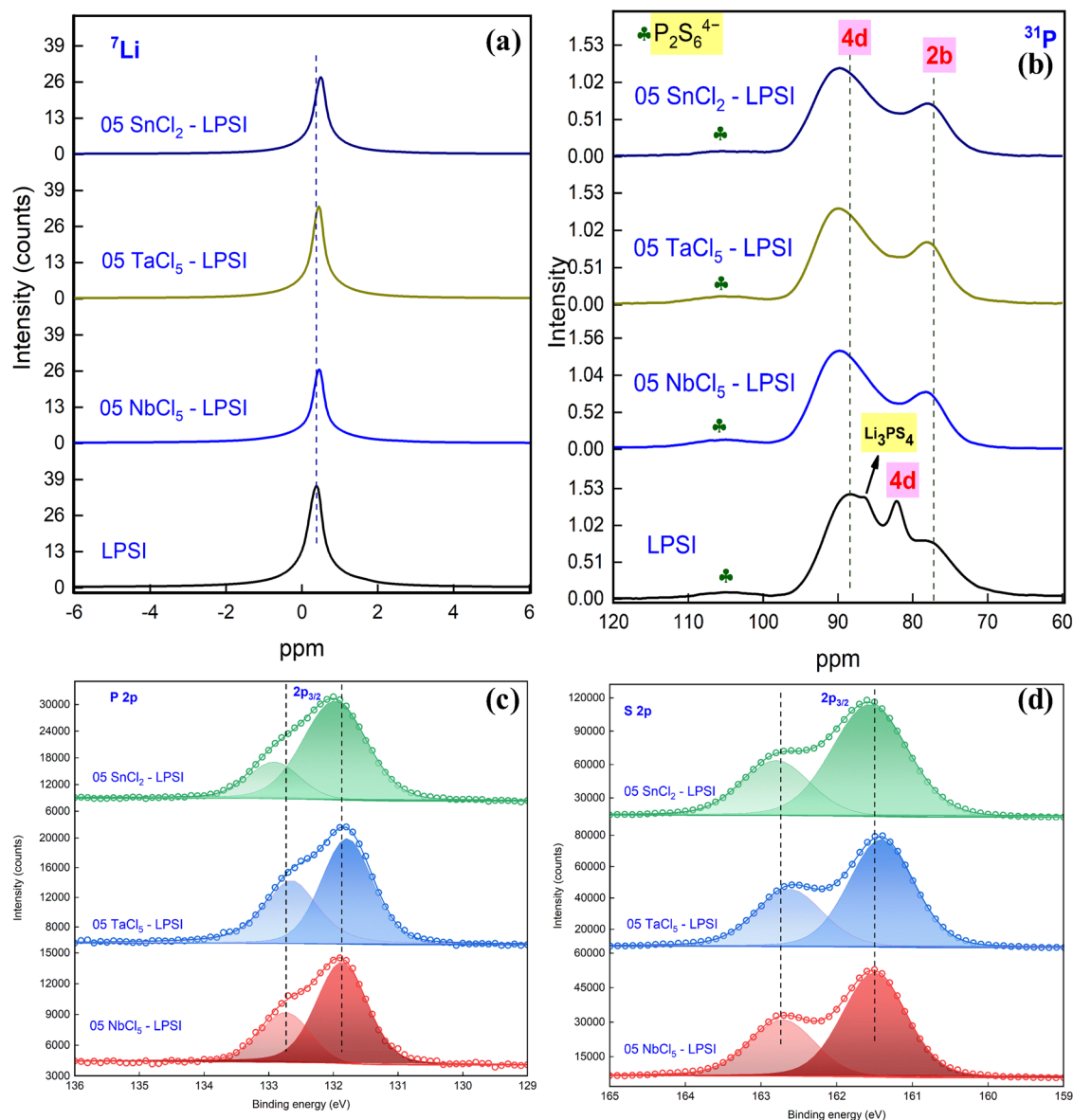


Fig. 2 | Solid MAS NMR and XPS analysis of halide-doped LPSI solid electrolyte. a ^7Li MAS NMR, **b** ^{31}P MAS NMR spectra, deconvoluted XPS spectra of **c** P 2p and **d** S 2p of pure and metal halide doped LPSI solid electrolyte.

electrolyte; which disappeared after metal halide doping^{24,28–31}. Therefore, the solid NMR analysis also confirmed that the addition of metal halide promotes the formation of a high ionic conducting phase.

Moreover, the chemical state of LPSI and metal halide-doped LPSI solid electrolytes were studied by XPS analysis, and the respective P 2p and S 2p deconvoluted spectra are shown in Fig. 2c and d. The deconvoluted XPS spectrum of P 2p displays characteristic peaks at 131.8 eV and 132.6 eV that correspond to P 2p_{3/2}. Aside from the peak intensity, no significant changes were observed in NbCl₅- and TaCl₅-doped LPSI solid electrolytes. Interestingly, SnCl₂ doping showed a specific peak shift at the shoulder peak around 132.9 eV. This may be attributable to the influence of unequal valence (Sn²⁺) doping at the P-site, which disturbed the chemical state of the P element. Similarly, the deconvoluted XPS spectrum of S 2p shows the characteristic peaks observed at 161.5 eV and 162.7 eV that correspond to S 2p_{3/2}. Notably, no significant changes aside from the minor peak shift were observed in the S 2p spectra. This indicates that the metal halide doping influenced the P-site rather than the S-site. The characteristic peaks of P and S correspond to the PS₄³⁻ system. The deconvoluted XPS spectrum of Cl 2p shows the characteristic peaks at 198.5 eV and 200.2 eV. The deconvoluted

XPS spectrum of Nb 3d shows the characteristic peaks observed at 204.3 eV and 207 eV. The deconvoluted XPS spectrum of Ta 4f shows the characteristic peaks observed at 25.8 eV and 27.7 eV. The deconvoluted XPS spectrum of Sn 3d shows the characteristic peaks observed at 486.4 eV and 494.7 eV. The XPS spectra of Li 1s, I 3d, Cl 2p, Nb 3d, Ta 4f, and Sn 3d are shown in Supplementary Fig. S2. Here, it should be noted that the peak intensity of iodine decreased depending on chloride doping concentration. The FE-SEM images and EDS mapping images of the NbCl₅-, TaCl₅-, and SnCl₂-doped LPSI solid electrolytes are shown in Supplementary Fig. S3 to Supplementary Fig. S6. Nearly uniform-sized particles were observed with the average particle size ranging from 2 to 7 μm. Moreover, EDS mapping analysis also confirmed the presence of P, S, I, Nb, Ta, Sn, and Cl elements in the solid electrolytes.

Electrochemical analysis

The lithium-ion conductivity of the LPSI and metal halide-doped LPSI solid electrolytes were calculated from the electrochemical impedance spectroscopy analysis and the corresponding schematic diagram is shown in Fig. 3a. As shown in Fig. 3b, the total ionic conductivity of the solid electrolytes was

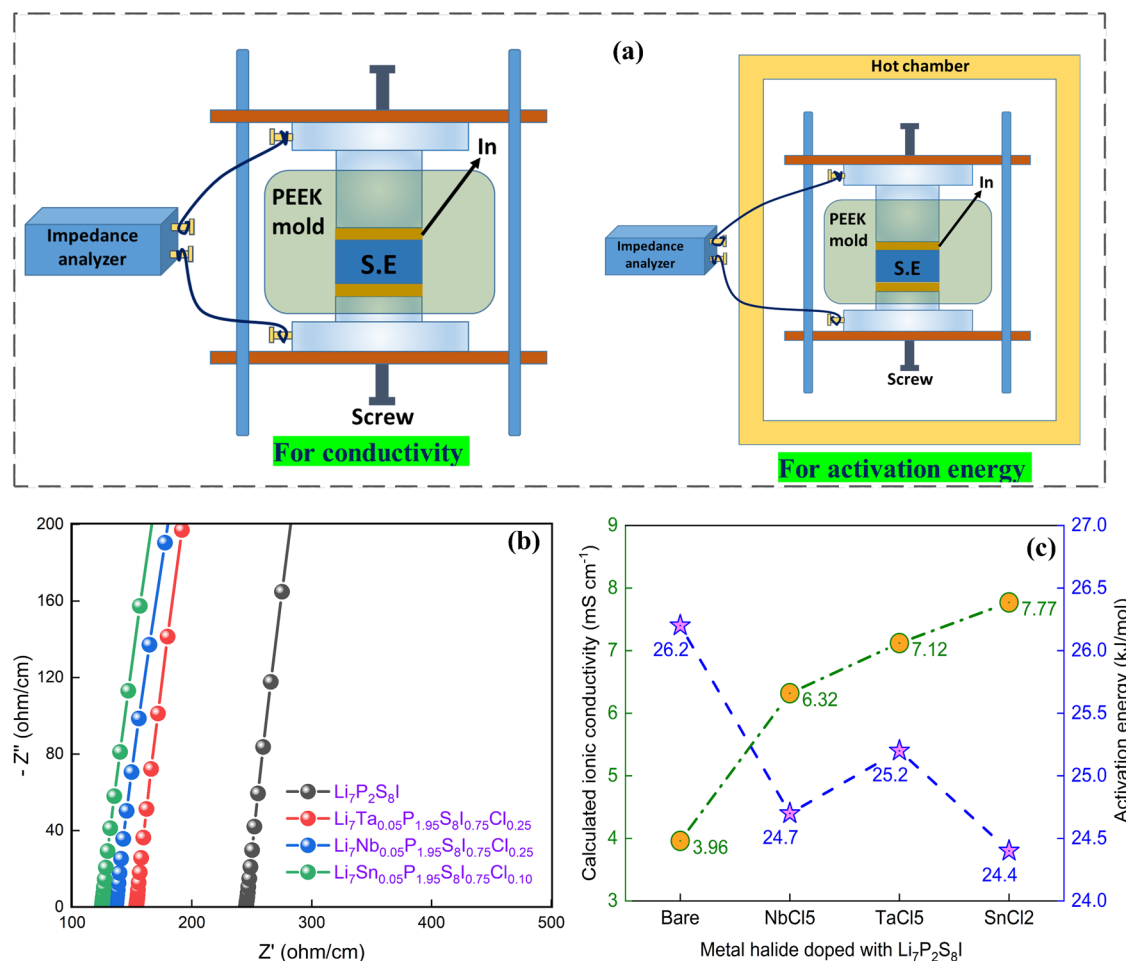


Fig. 3 | Ionic conductivity analysis of halide-doped LPSI solid electrolyte. a schematic diagram of impedance analysis, **b** Nyquist spectra, **c** calculated ionic conductivity, and activation energy value of pure and metal halide-doped LPSI solid electrolyte.

calculated from the resistance value at the intersection between the and the x-axis (full spectra is shown in Supplementary Fig. S7). The calculated ionic conductivity of LPSI solid electrolyte is $3.96 \times 10^{-3} \text{ S cm}^{-1}$. The ionic conductivity of the metal halide-doped LPSI solid electrolyte exhibits a higher value than the LPSI solid electrolyte. The calculated ionic conductivities of NbCl₅, TaCl₅, and SnCl₂-doped LPSI solid electrolytes are 6.32, 7.12, and 7.77 mS cm⁻¹, respectively. In this case, the doped metal cations may replace/occupy the P-site, and the halide anions are distributed over the crystal lattice. The calculated ionic conductivity of the solid electrolytes is shown in Fig. 3. Further, the metal halide doping with heat treatment promotes the formation of dominant thio-LISICON phase II and the combination of these different crystalline phases is the reason for this improved ionic conductivity. We also calculated the activation energy of the solid electrolytes by measuring the ionic conductivity at different temperatures (30 °C to 100 °C), and the corresponding Nyquist plots are included in Supplementary Fig. S8. The calculated activation energy from Fig. 3c suggests that the metal halide doping substantially decreased the activation energy of the solid electrolytes. The corresponding activation energy graph is shown in Supplementary Fig. S9.

The electrochemical window stability of the solid electrolytes was studied using cyclic voltammetry techniques, and the corresponding graphs are shown in Fig. 4a. In all the solid electrolytes, we observed cathodic and anodic peaks respectively corresponding to the occurrence of Li deposition and dissolution, respectively. No other major oxidation-reduction peaks were observed in the CV graph, thus confirming good electrochemical reversibility. Unfortunately, a minor S²⁻ anodic peak was observed in TaCl₅-doped LPSI solid electrolyte, large atomic size might be the reason for this

impurity peak. The critical current density analysis of the prepared solid electrolytes was conducted using a DC polarization method to evaluate the stability against lithium metal with cell configuration of Li/solid electrolyte/Li symmetry cell, and the corresponding graph is shown in SI. This critical current density value is used to understand the interface stability of solid electrolytes with lithium metal anode and also the reversibility over lithium stripping/plating at different current densities. The measured critical current density value of the prepared LPSI solid electrolyte is 0.35 mA cm⁻². The critical current density values were improved substantially after metal halide doping, and the measured critical current density values of NbCl₅-, TaCl₅-, and SnCl₂-doped LPSI solid electrolyte are 0.4, 0.5, and 1.0 mA cm⁻², respectively (Fig. 4b, Supplementary Fig. S10). This suggests that the addition of metal halides significantly enhanced the stability of the solid electrolytes against the lithium metal. More specifically, SnCl₂-doped solid electrolyte exhibits high stability, because the Sn cation reacts with lithium metal and produces Li-Sn alloys. This Li-Sn alloy suppresses the lithium dendrite growth and enhances the stability of the solid electrolytes against lithium metal. Interestingly, at a low applied current density (0.1 mA g⁻¹), both the bare LPSI and SnCl₂-doped LPSI solid electrolytes exhibit good stability up to 100 cycles. When further increasing the applied current density to 0.2 mA g⁻¹, the bare LPSI solid electrolytes became unstable (short circuit) at the 27th cycle (Supplementary Fig. S11). As was expected from the critical current density results, SnCl₂-doped LPSI solid electrolytes show high stability even after 100 cycles (Fig. 4c and d). Thus the formation of Li-Sn alloy with LiI additive is highly helpful with the suppression of Li dendrite growth. The formation of Li-Sn alloy during the interfacial reaction at the solid electrolyte and the lithium metal anode was confirmed by XPS analysis

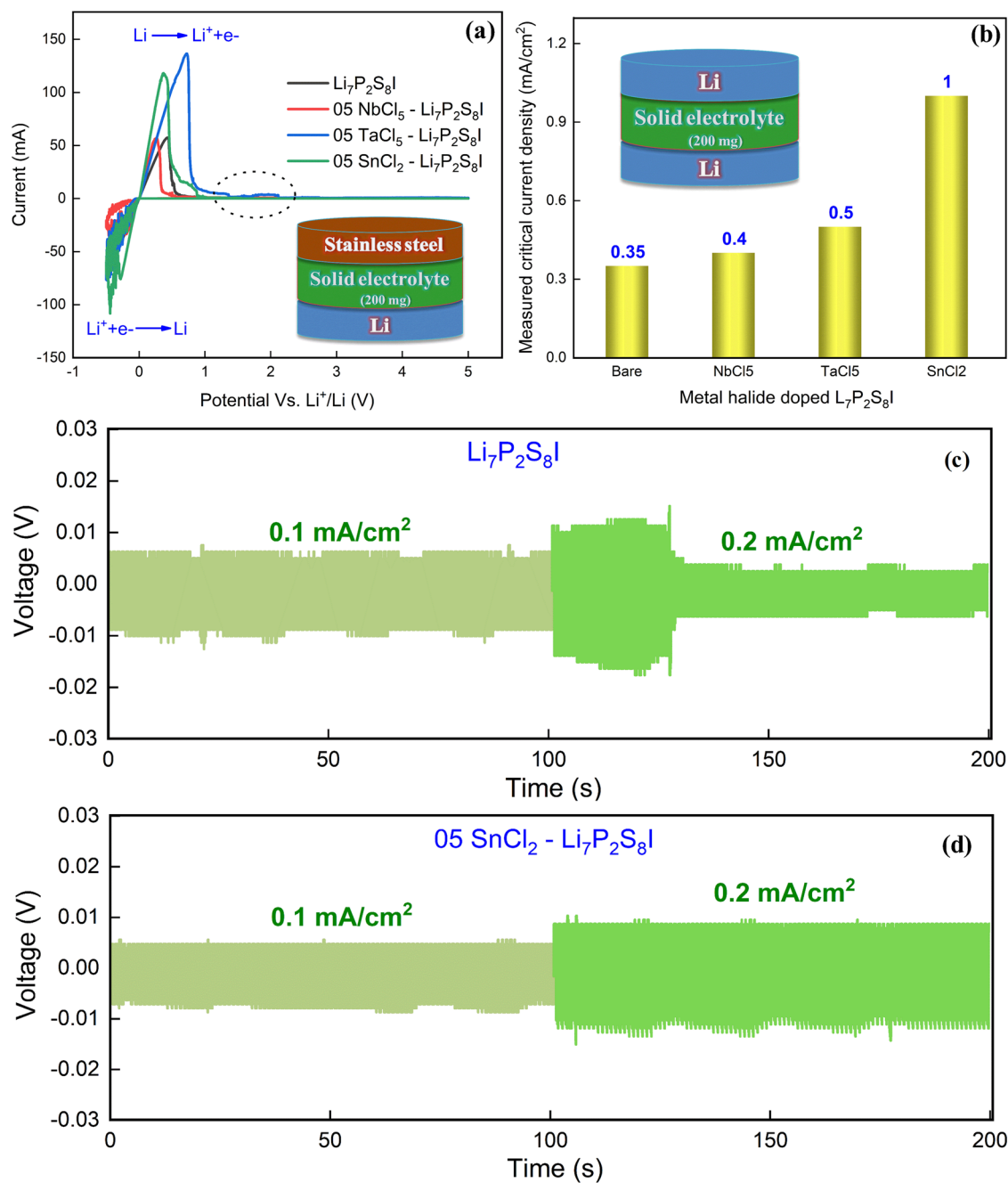


Fig. 4 | Electrochemical stability analysis of halide-doped LPSI solid electrolyte. a Cyclic voltammetry graph, **b** calculated critical current density value of pure and metal halide-doped LPSI solid electrolyte, long time DC cycle graph of **c** LPSI and **d** SnCl₂-doped LPSI solid electrolyte at the applied current density value of 0.1 mA cm⁻².

after the DC cycle stability test. Figure 5a and b show the XPS spectra of Li 1s and Sn 3d elements before and after DC cycling at 0.1 mA/cm² applied current density. In Li 1s spectra, we observed the characteristic peak's broadening and the existence of a new peak at 56.4 eV. This new peak belongs to the formation of Li-Sn alloy³². Further, we also observed the peak shift in Sn 3d spectra confirming the formation of Li-Sn alloy. Figure 5c shows the schematic diagram of Li dendrite suppression during the electrochemical reaction.

Finally, we have fabricated the all-solid-state lithium battery (ASSBs) using the selected SnCl₂ doped LPSI solid electrolytes, and we conducted the charge-discharge analysis of Li/solid electrolyte/NCM composite asymmetric cells at a 0.1 C-rate (1 C = 200 mAh g⁻¹)³³. The fabricated solid-state lithium battery cell was charged up to 4.3 V and discharged to the cut-off voltage of 2.6 V. The fabricated asymmetric Li/Li₇P₂S₈I/NCM composite

(Cell-1) exhibited a charge capacity of 231.7 mAh g⁻¹ and a discharge capacity of 161.7 mAh g⁻¹ at room temperature. The initial discharge capacity of Cell - 1 shows 80% utilization of the theoretical capacity of NMC811 (200 mAh g⁻¹) with 69.8% columbic efficiency. This high utilization suggests that the prepared solid electrolyte provided excellent electronic and ionic pathways in the cathode composite. After the first cycle, the charge capacities were nearly equal to the discharge capacities. The fabricated asymmetric Cell-1 also exhibited good cycle stability and showed 88% specific discharge capacity retention after 100 cycles. To further improve the performance of ASSB, we have removed the conducting agent (Super-P) during the cathode composite preparation and mixed the cathode active material (NCM811) and solid electrolyte (Li₇P₂S₈I) at a respective ratio of 70:30. The cathode material was already coated with LiNbO₃ material, which has significant electronic conductivity. Moreover, removing the

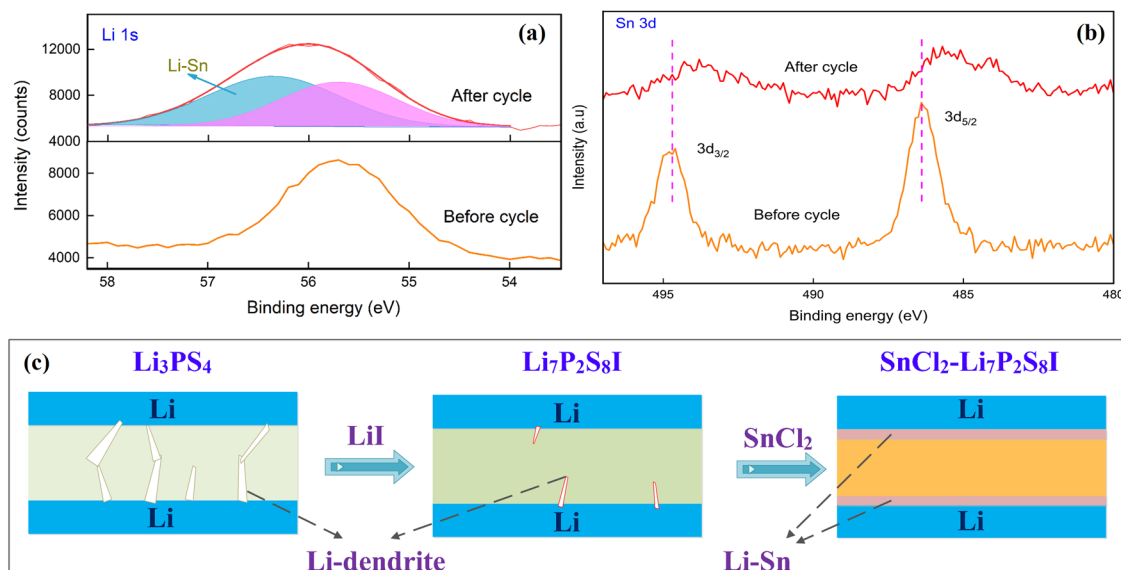


Fig. 5 | Conformation of interlayer formation. XPS spectra of **a** Li 1s and **b** Sn 3d of SnCl₂ doped LPSI solid electrolyte at before and after DC cycling, and **c** schematic diagram of Li dendrite suppression during the electrochemical reaction.

conducting agent may reduce the decomposition kinetics of our electrolytes and increase the columbic efficiency¹⁷. Thus, we have assembled different all-solid-state lithium batteries using LPSI and SnCl₂-doped LPSI solid electrolytes, and the corresponding combinations are presented in Supplementary Fig. S12. Before charge-discharge analysis, the EIS analysis was performed for all fabricated ASSBs and the corresponding Nyquist plot is shown in Supplementary Fig. S13. As a result, the fabricated asymmetric Cell - 2 exhibited the initial discharge capacity value of 168.5 mAh g⁻¹ with 74.2% columbic efficiency at room temperature. This initial specific discharge capacity value improved when using the SnCl₂-doped LPSI solid electrolyte, and the initial cycle discharge capacity values of Cell - 3 and Cell - 4 are 180 mAh g⁻¹ and 183.3 mAh g⁻¹ at 0.1 C-rate with the first cycle columbic efficiencies of 74.3% and 72.3%, respectively. The cycle stability value also improved for Cell - 2, Cell - 3, and Cell - 4 to 92.1%, 97.3% and 98.6%, respectively, after 100 cycles. This clearly indicated that the addition of metal halide highly enhanced the electrochemical performances. The corresponding initial cycle charge-discharge curve, 100th cycle charge-discharge curve, and cycle stability graph are shown in Fig. 6a, b, and c, respectively. Thus the observed specific capacity, columbic efficiency, and the cycle stability value of SnCl₂-doped LPSI solid electrolyte-based ASSB is much higher than reported Li₇P₂S₈X-based solid electrolytes and other argyrodite-based ASSBs^{14,34,35}. We also studied the C-rate performance of the fabricated Cell - 1 to Cell - 4, and the corresponding graph is shown in Fig. 6d. While increasing the C-rate to 0.2 C, 0.5 C, and 1 C, the specific capacity gradually decreased, the scan rate again decreased to 0.1 C, and the specific capacity returned to its original value. Compared to the LPSI solid electrolyte-based ASSBs (Cell - 1 and Cell - 2), SnCl₂-doped LPSI solid electrolyte-based ASSBs show better C-rate performances.

The DC polarization analysis and the charge-discharge analysis proved that the metal halide doping not only improved the ionic conductivity of the solid electrolyte but also improved the interfacial stability. Thus, we have studied the interfacial stability through long charge-discharge cycle analysis and post-electrochemical impedance spectroscopy analysis. After 100 cycles of CD analysis at a 0.1 C-rate, the C-rate was increased to 0.5 C and the charge-discharge cycle analysis was conducted for 250 cycles (Fig. 7). At a 0.5 C-rate, Cell - 1 showed immediate minor short circuit that was attributed to dendrite growth. Further increasing the CD cycles, the specific discharge capacity continued decreasing and showed 79.8% specific capacity retention after 250 cycles. In the case of carbon-free cathode composite (Cell - 2), the fabricated ASSB managed to run up to 100 cycles. Then, a short

circuit was observed, and the cell managed to run for up to ~ 240 cycles without a major short circuit. SnCl₂-doped LPSI solid electrolyte-based Cell - 3 and Cell - 4 both exhibit excellent cyclic stability up to 250 cycles without major discharge capacity fade, and the calculated specific capacity retention values are 98.8% and 99.2%, respectively.

After charge-discharge analysis (250 cycles), we performed electrochemical impedance to understand the interfacial stability of the ASSBs. The EIS experiment was conducted between the frequency of 1 MHz to 0.01 Hz at room temperature. Compared to Cell - 1 and Cell - 2, SnCl₂-doped LPSI solid electrolyte-based ASSBs exhibited high stability during the galvanostatic charge-discharge cycles. Specifically, Cell - 4 exhibits very low interfacial resistance, which is attributed to its high stability against lithium metal and cathode active materials. The respective Nyquist plots and the calculated resistance values are respectively presented in Fig. 8a and Table 1. Thus the calculated resistant components were classified in to bulk resistance of solid electrolyte (R1), grain boundary resistance of solid electrolyte (R2), interface resistance between solid electrolyte and cathode (R3), and the interface resistance between solid electrolyte and anode (R4)³⁶. Compared to Cell - 1, the resistance value of Cell - 2 is high indicating poor electronic conductivity without conducting agent (super - P). Interestingly, Cell - 3 and Cell - 4 show relatively low resistance values confirming the compatibility of SnCl₂-doped LPSI solid electrolyte for the fabrication of ASSBs. Specifically, interface resistance between solid electrolyte and anode at Cell - 4 is much lower than all other fabricated ASSBs further confirming the stability of SnCl₂-doped LPSI solid electrolyte against lithium metal anode. We also conducted Galvanostatic intermittent titration technique (GITT) measurements to study the diffusion coefficient value with an applied pulse current of 0.1 C for 10 minutes along with rest for 90 minutes to reach the steady state. The charging was continued until reaching the voltage of 4.3 V. Then, the discharge process was carried out with a pulse current of 0.1 C for 600 s and with rest for 90 minutes to reach a steady state. Figure 8b shows the GITT graph of Cell - 2, Cell - 3, and Cell - 4. The lithium diffusion coefficient value of the ASSBs was calculated from the following Eq. (1) [43]:

$$D_{Li^+} = \frac{4}{\pi\tau} \left(\frac{m_B V_M}{M_B A} \right)^2 \left(\frac{\Delta E_S}{\Delta E_T} \right)^2 \quad (1)$$

Where τ is pulse duration (600 s), m_B is the mass of the electrode material in the sample (0.0035 g), V_M is the molar volume of the sample (69.60 cm³ mol⁻¹), M_B is the molecular weight of the host sample

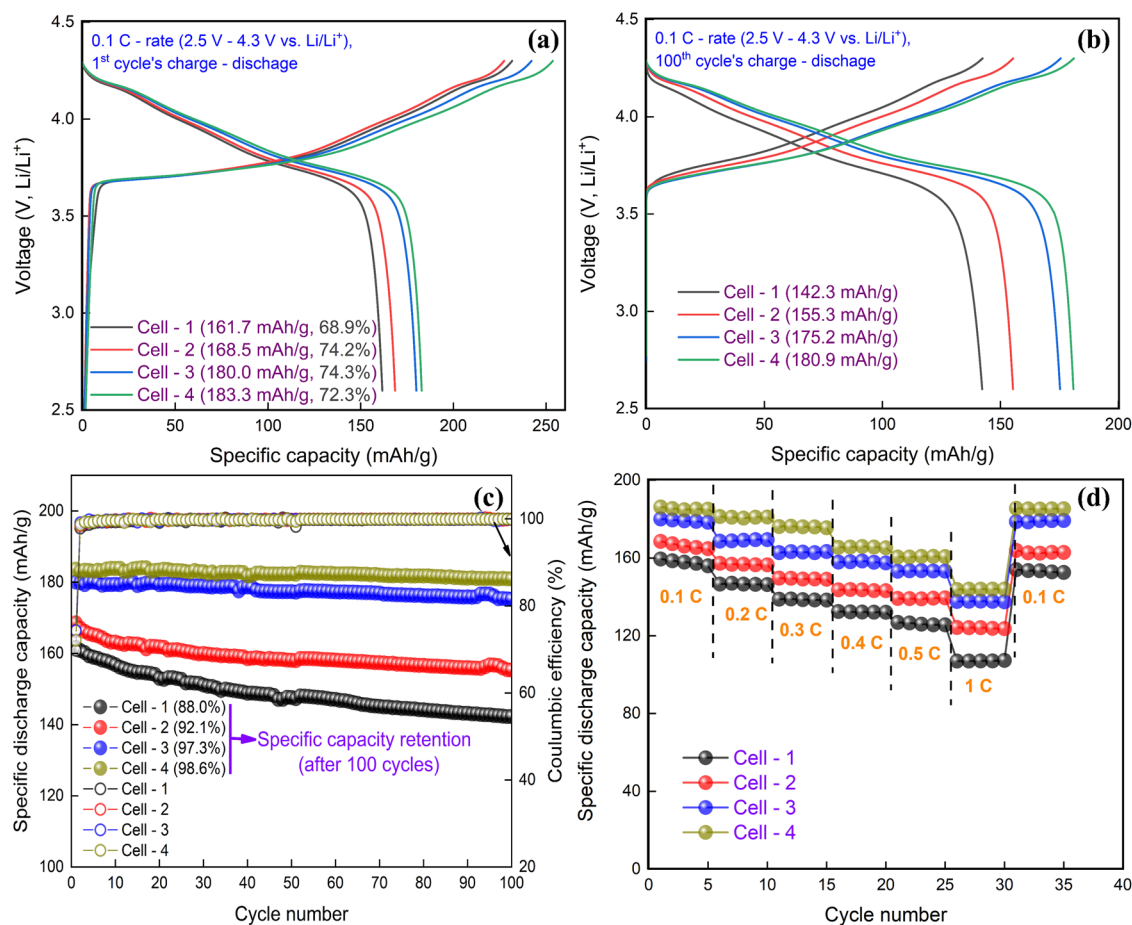
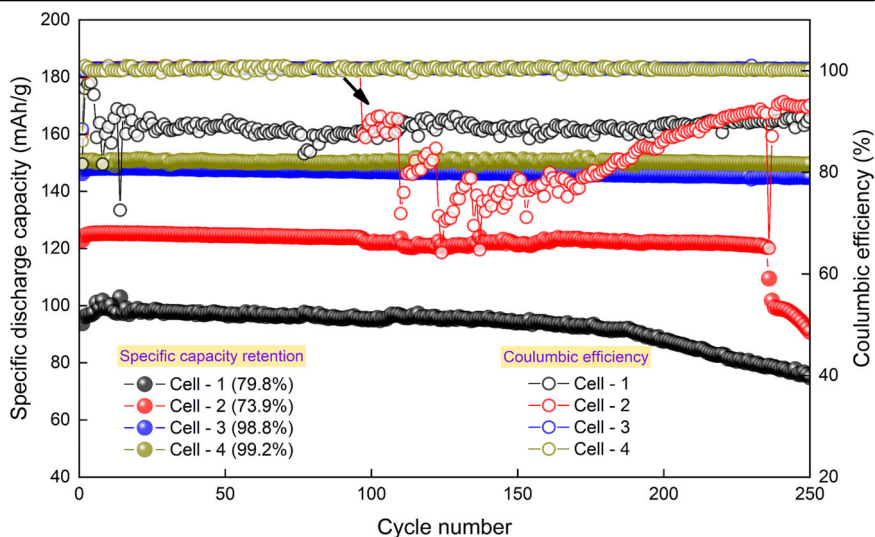


Fig. 6 | Galvanostatic charge-discharge analysis. Charge-discharge graph of **a** initial cycle, **b** 100th cycle, **c** charge-discharge long cycle stability graph, and **d** C-rate performance graph of fabricated ASSBs at room temperature.

Fig. 7 | Galvanostatic charge-discharge cycle stability analysis. CD long cycle graph of fabricated ASSBs at a 0.5 C-rate.



(NCM = 96.93 g mol⁻¹), A is the contact area between the electrolyte and active materials (2.01 cm²), ΔE_s is the steady-state voltage change, and ΔE_t is the transient voltage change.

The calculated lithium diffusion coefficient values of Cell - 2, Cell - 3, and Cell - 4 were 9.9724 × 10⁻⁹, 11.0597 × 10⁻⁹, and 10.4587 × 10⁻⁹ cm² s⁻¹, respectively. This confirmed that SnCl₂ not only improved ionic conductivity but also enhanced the lithium diffusion coefficient.

For more understanding of the interfacial resistance, in-situ impedance analysis and the corresponding distribution of relaxation time (DRT) were performed for Cell - 2 and Cell - 4, at their first cycle's state of charge (0, 25, 50, 75, and 100%) and depth of discharge (100, 75, 50, 25 and 0%) process^{20,37}. The charge-discharge process was carried out between the potential of 2.6 V to 4.3 V against a lithium metal anode with 0.1 C - rate. During the charging process, Cell - 4 shows high diffusion than bare LPSI

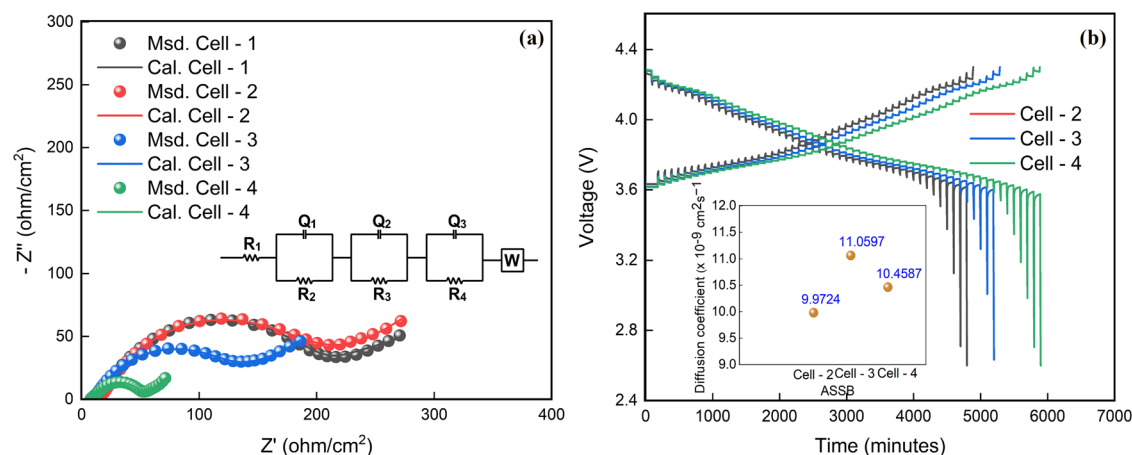


Fig. 8 | Post charge-discharge analysis. a EIS spectra and b GITT graph of fabricated ASSBs after charge-discharge cycles.

solid electrolyte-based Cell – 2. The EIS spectra confirmed that the total resistance of Cell – 4 is smaller than that Cell – 2, which indicates the stability of SnCl_2 -doped LPSI solid electrolyte against electrochemical reaction. According to the DRT calculation, the bulk resistance (R_1) value is gradually decreased during the charging process and increased during the discharging process in Cell – 2 and Cell – 4. Cumulatively, SnCl_2 -doped LPSI solid electrolyte exhibits less grain boundary resistance (R_2) and electrolyte–cathode interface resistance (R_3) than LPSI solid electrolyte during the charge-discharge process. Further, the DRT calculation confirmed that the electrolyte-anode interface resistance (R_4) is much reduced while using the SnCl_2 -doped LPSI solid electrolyte in ASSBs. This is further evident that the prepared SnCl_2 -doped LPSI solid electrolyte is highly stable against lithium metal anode and suitable for high energy density ASSB fabrication. For more detailed understanding, we also plotted the 2D intensity DRT color map. The obtained Nyquist spectra, DRT curve, and the DRT 2D mapping of Cell – 2 and Cell – 4 at various charging and discharging states are shown in Fig. 9.

Based on the C-rate performance, charge-discharge analysis, and cycle stability analysis were conducted for Cell – 4 (fresh) at a high C-rate (1 C), and the corresponding graphs are shown in Fig. 10. For high C-rate (1 C) stability analysis, 2.5 mg of cathode material was used to fabricate the ASSB (Cell – 5) to avoid a short circuit according to critical current density analysis. Except for the cathode active materials loading, the Cell – 4 and Cell – 5 configurations are the same. The initial specific discharge capacity value of Cell – 5 is 176 mAh g^{-1} at a 1 C-rate. The specific capacity retention after 50 cycles is 94.7%. The obtained specific capacity and cycle stability values exceeded those of the $\text{Li}_7\text{P}_2\text{S}_8\text{X}$ -type solid electrolyte-based ASSBs. Therefore, the proposed mechanism would reduce the fabrication cost and enhance the performance of all-solid-state lithium-ion batteries, and this idea opens different routes toward the development of sulfide solid electrolytes. For comparison, we also prepared the SnCl_2 doped LPSI solid electrolyte-based ASSB with high cathode loading (20 mg), and the corresponding graphs are shown in Supplementary Fig. S14. Although the

prepared ASSB exhibited a good discharge capacity value of 116.9 mAh g^{-1} , the cycle stability is poor and short circuit at 8th cycle. Thus, some improvements/optimization are needed to achieve better performance with high electrode mass loading.

After CD analysis (Cell – 4), we studied the cathode-solid electrolyte interface through FE-SEM analysis. Before the FE-SEM analysis, the cross-section of the cathode interface was obtained using focused ion beam (FIB) technology. The corresponding FE-SEM image and EDS mapping are shown in Fig. 11. From the FE-SEM image, we observed cracks in the voids on the cathode active materials, which may be due to the applied pressure or volume expansion (due to electrochemical reaction). Interestingly, cathode-active materials were immersed in the solid electrolyte layer, thus indicating good contact. The EDS analysis clearly distinguishes the solid electrolyte layer and the cathode material layer with the presence of P, S, I, Ni, Co, Mn, and O elements. Unfortunately, Sn and Cl elements were not detected in the mapping, and the same results were seen in the EDS spectrum (Supplementary Fig. S15).

Dry-air stability analysis

Dry-air stability test analysis was performed for the LPSI and metal halide-doped LPSI solid electrolytes. After dry-air exposure, XRD analysis was conducted, and the corresponding patterns are presented in Fig. 12a. Interestingly, pure and metal halide-doped LPSI solid electrolytes did not show any impurity phase or decomposition after air exposure. This suggests that the prepared solid electrolytes exhibit good moisture stability against dry air. Further, metal halide-doped solid electrolytes exhibit slightly higher ionic conductivity retention values of 55.8%, 63.0%, and 58.4% than pure/undoped LPSI solid electrolytes (55.8%). The calculated ionic conductivity value of LPSI and metal halide-doped LPSI solid electrolytes after dry-air exposure are shown in Fig. 12b.

Conclusions

In this work, we have prepared metal halide-doped LPSI solid electrolyte using a high energy ball milling process with controlled particle size and high ionic conductivity. The prepared SnCl_2 -doped LPSI solid electrolyte exhibited a high ionic conductivity value of 7.77 mS cm^{-1} at room temperature. Further, the prepared SnCl_2 doped LPSI solid electrolyte exhibited electrochemical performances that were superior to that of bare LPSI solid electrolyte. As a result, our proposed SnCl_2 -doped LPSI solid electrolyte-based ASSB exhibited an excellent specific capacity value of 183.3 mAh g^{-1} (0.1 C rate) with 98.6% specific capacity retention after 100 cycles. Moreover, the proposed ASSB is capable of working at a high C – rate for a large number of cycles. Thus, metal halide (SnCl_2) doping is an effective way to improve the electrochemical performance of LPSI solid electrolyte and may open the door for future technological innovations.

Table 1 | Calculated resistance value of ASSBs Calculated impedance value of the fabricated ASSBs after charge-discharge cycles

ASSB	R1 (Ω)	R2 (Ω)	R3 (Ω)	R4 (Ω)	W ($\text{S s}^{0.5}$)
Cell – 1	17.35	14.58	82.82	387.9	0.04
Cell – 2	25.21	6.72	153.2	316.5	0.02
Cell – 3	15.58	6.34	36.15	242.7	0.03
Cell – 4	16.35	5.80	7.43	82.11	0.08

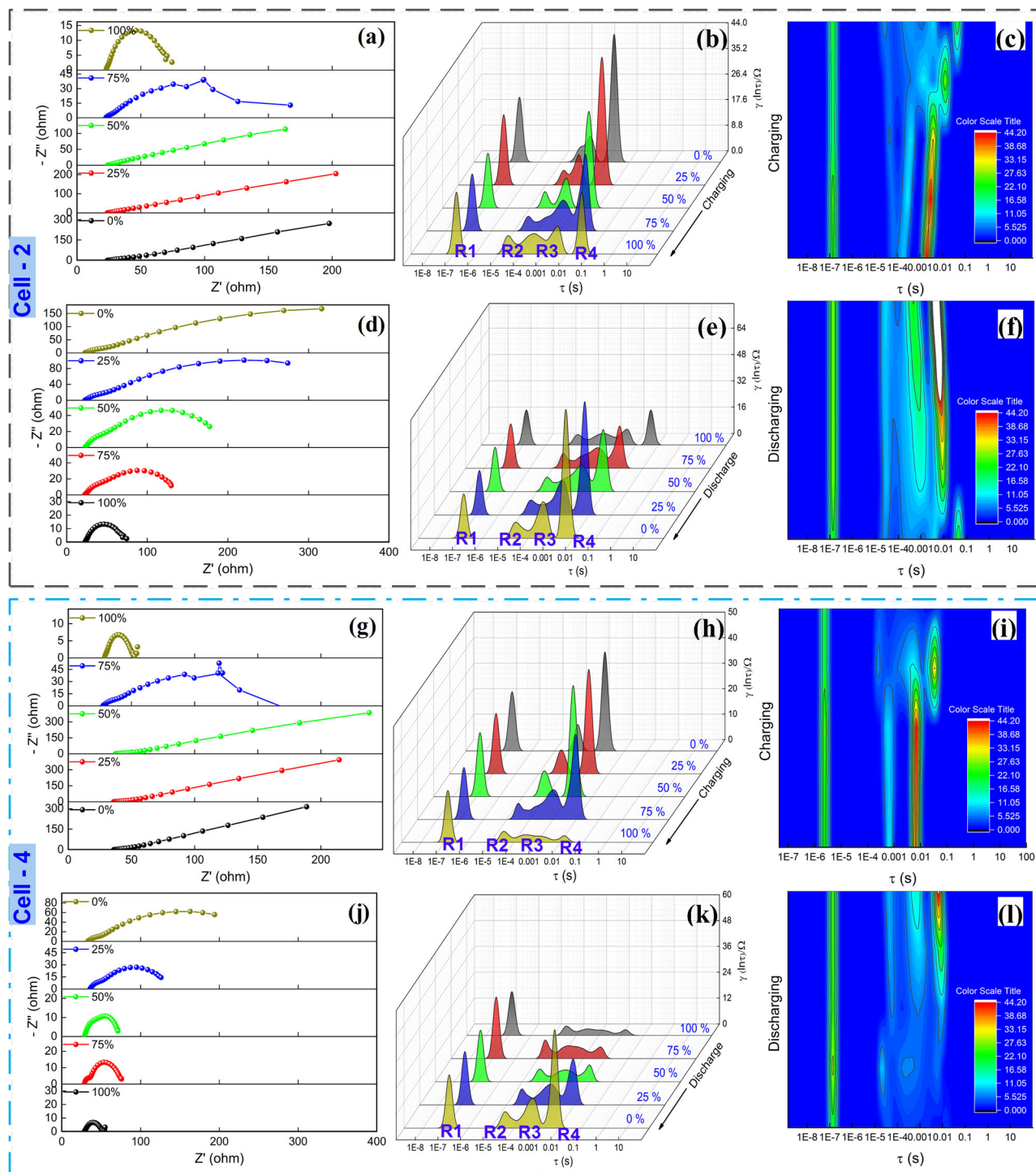


Fig. 9 | Detailed impedance analysis after charge–discharge cycles. a, g Nyquist plot, **b, h** calculated DRT curve and **c, i** 2D intensity color map of DRT curve of Cell – 2 and Cell – 4 at 1st cycle different charge states, **d, j** Nyquist plot, **e, k** calculated DRT curve and **f, l** 2D intensity color map of DRT curve of Cell – 2 and Cell – 4 at 1st cycle different discharge states.

Methods

Preparation of metal halide-doped $\text{Li}_7\text{P}_2\text{S}_8\text{I}$ solid electrolytes

First, $\text{Li}_7\text{P}_2\text{S}_8\text{I}$ solid electrolyte material was prepared through a high energy dry ball milling process using Li_2S (99.98%, Sigma Aldrich), P_2S_5 (99%, Sigma Aldrich), and LiI (99.999%, Sigma Aldrich) as starting material. All the source materials were used as received without any purification. Briefly, 0.6976 g of Li_2S , 1.125 g of P_2S_5 , and 0.6774 g of LiI were mixed in a respective molar ratio of 3:1:1. Next, the starting materials

were ground together for 15 minutes using a mortar and pestle and transferred to an 80 ml alumina planetary ball mill vessel. Then, 50 g of 6 mm zirconia balls and 25 g of 3 mm zirconia balls were added and sealed. At this point, the alumina vessel was brought out from the glove box and mounted on the ball mill machine (Pulverisette, Fritsch) and ball milled for 10 hours at 500 rpm. During the ball milling process, the rotation direction was changed every 20 minutes after 10 minutes of rest to avoid overheating and enhance the uniform mixing/milling. After the ball

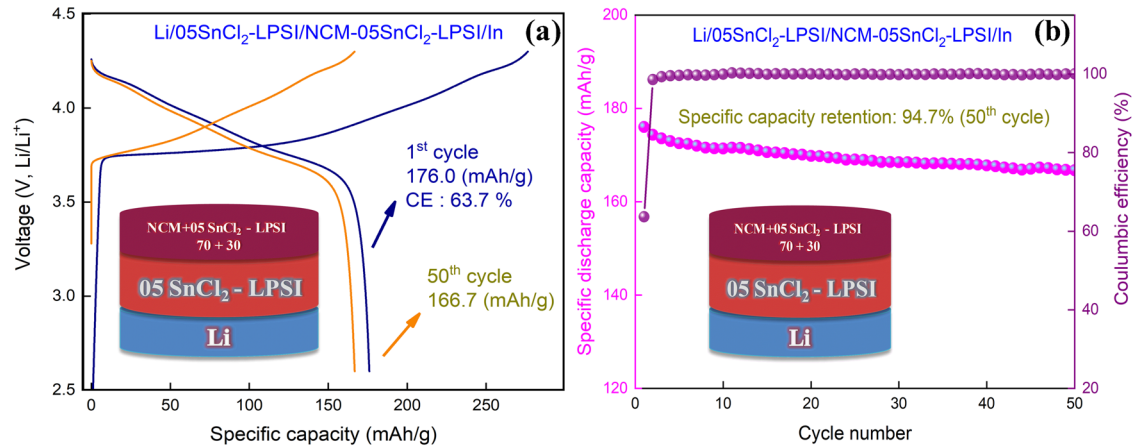


Fig. 10 | Galvanostatic charge- discharge analysis at high C-rate. a Charge-discharge graph and b cycle stability graph of fabricated ASSB at high C –rate.

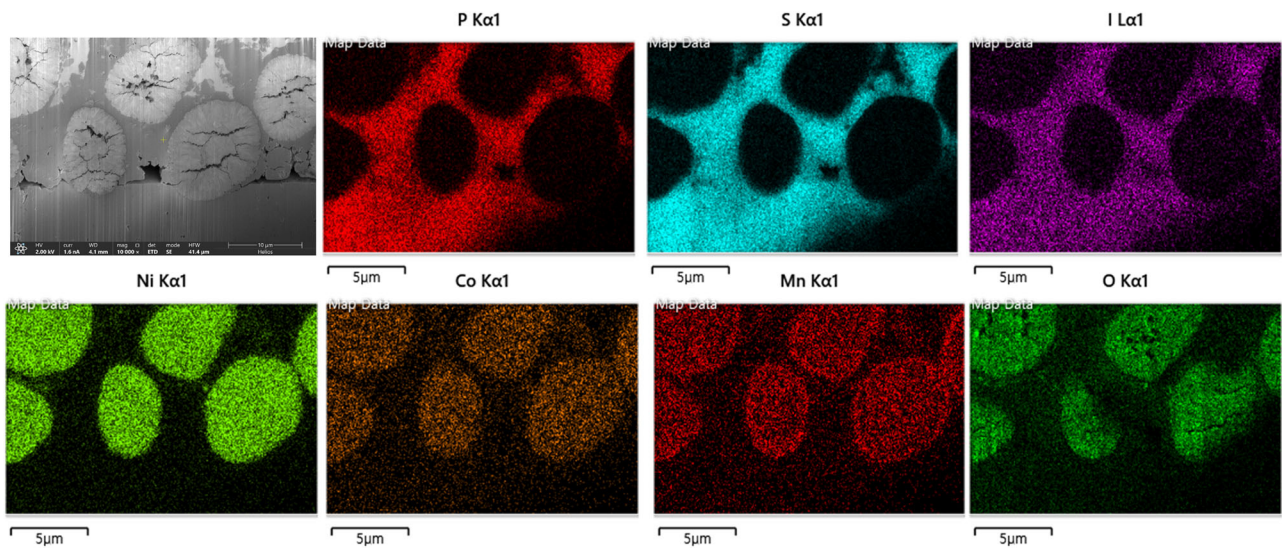


Fig. 11 | FIB analysis. FIB cross-section image and EDS mapping at electrolyte cathode interface of Cell - 4 with P, S, I, Ni, Co, Mn, and O elements.

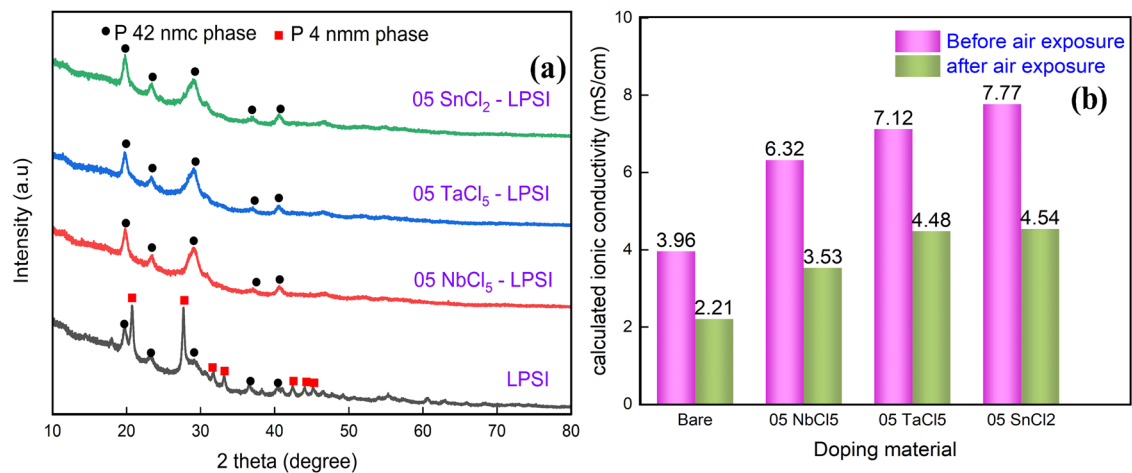


Fig. 12 | Dry-air stability analysis. a XRD pattern and b calculated ionic conductivity value of pure and metal halide-doped LPSI solid electrolyte after dry-air exposure.

milling process, the product was collected and ground for 15 minutes to obtain fine amorphous solid electrolyte powders. These obtained amorphous solid electrolytes is not suitable for lithium battery applications due to low ionic conductivity. Thus, the amorphous solid electrolyte was heat treated at 200 °C for 5 hours at a heating rate of 2 °C min⁻¹ to obtain a highly conductive crystalline solid electrolyte. The obtained solid electrolyte was Li₇P₂S₈I (LPSI). All the experiments were performed in an argon-filled glove box to protect from moisture.

The same experimental method was used to prepare metal halide-doped LPSI solid electrolytes; for instance, the starting materials of Li₂S (0.7569 g), P₂S₅ (1.1426 g), LiI (0.5292 g), and Nb₂Cl₅ (0.0712 g) were mixed in a respective molar ratio of 3.125:0.975:0.75:0.05. After a ball milling process, the product was collected and ground for 15 minutes to obtain fine amorphous solid electrolyte powders. Next, the amorphous solid electrolyte was heat treated at 200 °C for 5 hours at a heat rate of 2 °C min⁻¹. The obtained solid electrolyte was Li₇Nb_{0.05}P_{1.95}S₈I_{0.75}Cl_{0.25} (05 NbCl₅ – LPSI). Similarly, TaCl₅- and SnCl₅-doped LPSI solid electrolytes were prepared and named Li₇Ta_{0.05}P_{1.95}S₈I_{0.75}Cl_{0.25} (05 TaCl₅ – LPSI) and Li₇Sn_{0.05}P_{1.95}S₈I_{0.75}Cl_{0.10} (05 SnCl₂ – LPSI), respectively.

For comparison we also prepared 10 SnCl₂ – LPSI solid electrolytes using the same experimental method, for instance, the starting materials of Li₂S (0.7508 g), P₂S₅ (1.1042 g), LiI (0.5249 g), SnCl₂ (0.0991 g) and S (0.0209 g) were mixed with the molar ratio of 3.125:0.95:0.75:0.10:0.125. After the ball milling process, the product was collected and ground for 15 minutes to get fine amorphous solid electrolyte powders. Next, the amorphous solid electrolyte was heat treated at 200 °C for 5 hours with a heat rate of 2 °C min⁻¹. The obtained solid electrolyte will be Li₇Sn_{0.10}P_{1.90}S₈I_{0.75}Cl_{0.2} (10 SnCl₂ – LPSI).

Characterization

The crystalline nature and phase were studied utilizing an X-ray diffractometer (XRD, Rigaku-Ultima (IV)) using Cu K α radiation with a wavelength of 1.5418 Å. The solid electrolyte powder was loaded in an airtight XRD holder in an argon-filled glove box to avoid exposure to air or moisture. The XRD analysis was conducted within the 2 θ of 10 to 80° with the step size of 0.01 s⁻¹. Laser Raman spectroscopy analysis was performed with the excitation wavelength and power for the laser source were 532 nm and 8 mW, respectively. Nuclear magnetic resonance spectroscopy (NMR, VARIAN, VNMRS 600) was used to study ⁷Li and ³¹P chemical shifts. The frequency of 40 kHz was used for analysis. The active surface functional group of the electrolytes was studied by X-ray photoelectron spectroscopy (XPS) with a focused Al K α (1.487 keV) monochromator in an argon atmosphere. The analyzed area had a spot size of 500 μ m. The surface morphology and elemental distribution of the material were obtained using a field-emission scanning electron microscope coupled with an EDS instrument (FE-SEM, JSM-7610F, Japan). For dry-air stability analysis, the prepared solid electrolyte (500 mg) was placed in a 500 ml closed container filled with dry air and maintained at conditions of 13% humidity and 22% oxygen. The dry-air exposure analysis test was performed at 30 °C and the solid electrolyte sample was collected after 6 hours of dry-air exposure.

The total ionic conductivity of the solid electrolytes was measured by electrochemical impedance spectroscopy (EIS) using Biologic SP 300 between the frequencies of 7 MHz to 1 Hz at room temperature (25 °C). The ionic conductivity of the solid electrolyte was calculated using the equation $\sigma = \frac{d}{R \times A}$, where d is the thickness of the pellet, A is the area of the contact surface, and R is the total resistance measured from the Nyquist plot. Before the analysis, the sample (250 mg) was pressed into a pellet with a diameter of 10 mm and a thickness from 0.16 to 0.18 mm using hydraulic pressure (SANSO, HP-3S) with an applied pressure of 30 MPa. During the pressing, we attached 50 μ m of indium foil blocking electrode on both sides to ensure high contact and assembled it in a pressure cell. The electrochemical window stability of the solid electrolyte with lithium metal anode was studied by a CV technique using Li/solid electrolyte/stainless steel 2032-type asymmetric cell. The CV experiment was carried out between the

voltage of – 0.5 to 5 V with a 0.1 mV s⁻¹ scan rate using Biologic SP 300. For the critical current density analysis, a 2032-type coin cell was prepared in an argon-filled glove box at a current density of 0.05 mA cm⁻² to 1.2 mA cm⁻² with a duty cycle of 30 minutes using a MACCOR-battery analyzing system. Prior to the measurement, an electrolyte pellet (0.2 g, 16 mm diameter and ~1 mm thickness) was placed between the lithium metal anodes assembled in a 2032-type Li/solid electrolyte/Li symmetry coin cell. Finally, all solid-state lithium batteries (ASSBs) were assembled for various electrochemical analyses: First, the cathode composite was prepared by mixing LiNbO₃ coated LiNi_{0.8}Co_{0.1}Mn_{0.1}O₂ (NCM), the solid electrolyte, and super-P at a respective weight ratio of 70:28:2 and ground with a mortar and pestle. To fabricate the pellet-type coin cell, 0.2 g of solid electrolyte was pressed into a pellet with a diameter of 16 mm and a thickness of ~ 1 mm by applying the pressure of 50 MPa. Then, the prepared cathode composite (5.5 mg) was spread over one side of the electrolyte and covered with 50 μ m thick indium foil and pressed with 40 MPa. Finally, lithium foil was attached to the other side of the pellet with 10 MPa pressure. Then, the entire pellet was assembled in a 2032 type coin cell for further analysis. We performed electrochemical impedance spectroscopy analysis, cyclic voltammetry analysis, and galvanostatic charge-discharge analysis of the assembled ASSBs.

Supporting Information

Experimental, XRD pattern, XPS spectra, Laser Raman, impedance analysis, critical current density analysis, FESEM-EDS, CV, and charge-discharge graph of prepared solid electrolytes are presented.

Data availability

The authors declare that the data supporting the findings of this study are available within the paper and its supplementary information files.

Received: 23 December 2023; Accepted: 29 April 2024;

Published online: 18 May 2024

References

- Zeng, D. et al. Promoting favorable interfacial properties in lithium-based batteries using chlorine-rich sulfide inorganic solid-state electrolytes. *Nat. Commun.* **13**, 1909 (2022).
- Wang, D. et al. Realizing high-capacity all-solid-state lithium-sulfur batteries using a low-density inorganic solid-state electrolyte. *Nat. Commun.* **14**, 1895 (2023).
- Fu, F. et al. Unveiling and alleviating chemical “Crosstalk” of Succinonitrile molecules in hierarchical electrolyte for high-voltage solid-state lithium metal batteries. *Energy Environ. Mater.* **6**, e12367 (2023).
- Chen, H. et al. 20 mS cm⁻¹ Li-argyrodite solid electrolyte produced via facile high-speed-mixing. *Chem. Commun.* **59**, 7220–7223 (2023).
- Wu, Z. et al. Ag-modification argyrodite electrolytes enable high-performance for all-solid-state lithium metal batteries. *Chem. Eng. J.* **466**, 143304 (2023).
- Subramanian, Y., Rajagopal, R., Kang, S. & Ryu, K.-S. Optimization of high ionic conducting Br-rich and metal (Sb and Zr) substituted Li-argyrodite and their enhanced air stability and compatibility in lithium batteries. *Scr. Mater.* **235**, 115592 (2023).
- Feng, Q., Xie, X., Zheng, B. & Liao, N. Superior effect of Si doping on interfacial reaction of LiPON solid electrolyte for the Silicon-Rich Oxide (SiO_{1/2}) anode in all-solid-state batteries: a first-principles prediction. *ACS Appl. Energy Mater.* **6**, 2698–2706 (2023).
- Indrawan, R. F., Gamo, H., Nagai, A. & Matsuda, A. Chemically understanding the liquid-phase synthesis of argyrodite solid electrolyte Li₆PS₅Cl with the highest ionic conductivity for all-solid-state batteries. *Chem. Mater.* **35**, 2549–2558 (2023).
- Calpa, M. et al. Chemical stability of Li₆PS₄I solid electrolyte against hydrolysis. *Appl. Mater. Today* **22**, 100918 (2021).

10. Yu, C. et al. Enabling ultrafast ionic conductivity in Br-based lithium argyrodite electrolytes for solid-state batteries with different anodes. *Energy Storage Mater.* **30**, 238–249 (2020).
11. Rangasamy, E. et al. An iodide-based $\text{Li}_7\text{P}_2\text{S}_8\text{I}$ superionic conductor. *J. Am. Chem. Soc.* **137**, 1384–1387 (2015).
12. Wu, Z. et al. Engineering high conductive $\text{Li}_7\text{P}_2\text{S}_8\text{I}$ via Cl- doping for all-solid-state Li-S batteries workable at different operating temperatures. *Chem. Eng. J.* **442**, 136346 (2022).
13. Rajagopal, R. et al. Preparation of highly conductive metal doped/substituted $\text{Li}_7\text{P}_2\text{S}_8\text{Br}_{(1-x)}\text{I}_x$ type lithium superionic conductor for all-solid-state lithium battery applications. *Chem. Eng. J.* **428**, 132155 (2022).
14. Rajagopal, R., Subramanian, Y., Jung, Y. J., Kang, S. & Ryu, K.-S. Preparation of metal-oxide-doped $\text{Li}_7\text{P}_2\text{S}_8\text{Br}_{0.25}\text{I}_{0.75}$ solid electrolytes for all-solid-state lithium batteries. *ACS Appl. Mater. Interfaces* **15**, 21016–21026 (2023).
15. Naik, K. G., Chatterjee, D. & Mukherjee, P. P. Solid electrolyte–cathode interface dictates reaction heterogeneity and anode stability. *ACS Appl. Mater. Interfaces* **14**, 45308–45319 (2022).
16. Zou, C. et al. Stabilized cathode/sulfide electrolyte interface through conformally interfacial nanocoating for all-solid-state batteries. *ACS Appl. Energy Mater.* **6**, 3599–3607 (2023).
17. Zhao, F. et al. Tuning bifunctional interface for advanced sulfide-based all-solid-state batteries. *Energy Storage Mater.* **33**, 139–146 (2020).
18. Wu, L., Liu, G., Wan, H., Weng, W. & Yao, X. Superior lithium-stable $\text{Li}_7\text{P}_2\text{S}_8\text{I}$ solid electrolyte for all-solid-state lithium batteries. *J. Power Sources* **491**, 229565 (2021).
19. Taklu, B. W. et al. Dual CuCl doped argyrodite superconductor to boost the interfacial compatibility and air stability for all solid-state lithium metal batteries. *Nano Energy* **90**, 106542 (2021).
20. Liao, C. et al. Hunting highly conductive $\text{Li}_6\text{PS}_5\text{I}$ electrolyte via Sn-Cl dual doping for solid-state batteries. *Scr. Mater.* **226**, 115219 (2023).
21. Jang, G.-J., Rajagopal, R., Kang, S. & Ryu, K.-S. Preparation of argyrodite $\text{Li}_{6-2x}\text{Zn}_x\text{PS}_{5-x}\text{O}_x\text{Cl}$ with improved electrochemical performance and air stability for all-solid-state batteries. *J. Alloy. Compd.* **957**, 170273 (2023).
22. Gamo, H., Kusaba, I., Hikima, K. & Matsuda, A. Rapid solution synthesis of Argyrodite-Type $\text{Li}_6\text{PS}_5\text{X}$ (X = Cl, Br, and I) solid electrolytes using excess sulfur. *Inorg. Chem.* **62**, 6076–6083 (2023).
23. Wu, Z. et al. A comprehensive cognition for the capacity fading mechanism of FeS_2 in argyrodite-based all-solid-state lithium battery. *EcoMat* **5**, e12327 (2023).
24. Miß, V. et al. Heat treatment-induced conductivity enhancement in sulfide-based solid electrolytes: what is the role of the Thio-LISICON II Phase and of other nanoscale phases? *Chem. Mater.* **34**, 7721–7729 (2022).
25. Takahashi, M. et al. Investigation of the suppression of dendritic lithium growth with a lithium-iodide-containing solid electrolyte. *Chem. Mater.* **33**, 4907–4914 (2021).
26. Tan, D. H. S. et al. Elucidating reversible electrochemical Redox of $\text{Li}_6\text{PS}_5\text{Cl}$ solid electrolyte. *ACS Energy Lett.* **4**, 2418–2427 (2019).
27. Harm, S. et al. Lesson learned from NMR: Characterization and ionic conductivity of LGPS-like Li_7SiPS_8 . *Chem. Mater.* **31**, 1280–1288 (2019).
28. Sedlmaier, S. J. et al. $\text{Li}_4\text{PS}_4\text{I}$: A Li^+ superionic conductor synthesized by a solvent-based soft chemistry approach. *Chem. Mater.* **29**, 1830–1835 (2017).
29. Stöfler, H. et al. Li^+ -ion dynamics in $\beta\text{-Li}_3\text{PS}_4$ observed by NMR: Local hopping and long-range transport. *J. Phys. Chem. C.* **122**, 15954–15965 (2018).
30. Eckert, H., Zhang, Z. & Kennedy, J. H. Structural transformation of non-oxide chalcogenide glasses. The short-range order of lithium sulfide (Li_2S)-phosphorus pentasulfide (P_2S_5) glasses studied by quantitative phosphorus-31, lithium-6, and lithium-7 high-resolution solid-state NMR. *Chem. Mater.* **2**, 273–279 (1990).
31. Neuberger, S., Culver, S. P., Eckert, H., Zeier, W. G. & Günne, J. S. A. D. Refinement of the crystal structure of $\text{Li}_4\text{P}_2\text{S}_6$ using NMR crystallography. *Dalton Trans.* **47**, 11691–11695 (2018).
32. Wan, M. et al. Mechanical rolling formation of interpenetrated lithium metal/lithium tin alloy foil for ultrahigh-rate battery anode. *Nat. Commun.* **11**, 829 (2020).
33. Wei, J. et al. Enhanced electrochemical performance of cobalt oxide layers coated $\text{LiNi}_{0.8}\text{Co}_{0.1}\text{Mn}_{0.1}\text{O}_2$ by polyvinylpyrrolidone-assisted method cathode for Li-ion batteries. *J. Colloid Interface Sci.* **616**, 520–531 (2022).
34. Rajagopal, R., Subramanian, Y. & Ryu, K.-S. Preparation of $\text{Li}_7\text{P}_2\text{S}_8\text{X}$ -type solid electrolytes with complex anions for all-solid-state lithium battery applications. *ACS Sustain. Chem. Eng.* **11**, 2692–2703 (2023).
35. Yu, C. et al. Superionic conductivity in lithium argyrodite solid-state electrolyte by controlled Cl-doping. *Nano Energy* **69**, 104396 (2020).
36. Wei, C. et al. SnF_2 -induced multifunctional interface-stabilized $\text{Li}_{5.5}\text{PS}_{4.5}\text{Cl}_{1.5}$ -based all-solid-state lithium metal batteries. *Adv. Funct. Mater.* **34**, 2314306 (2024).
37. Hori, S. et al. Understanding the impedance spectra of all-solid-state lithium battery cells with sulfide superionic conductors. *J. Power Sources* **556**, 232450 (2023).

Acknowledgements

This study was supported by a National Research Foundation of Korea (NRF) grant (NRF-2019R1A6A1A11053838) funded by the Ministry of Education, Science and Technology (MEST) and (MSIT) (No. 2021R1A2C1011809) of the Korean Government.

Author contributions

Rajesh Rajagopal: Methodology, all experiments, Data analysis, Writing-original draft, review and editing, Yuvaraj Subramanian: Data analysis, Writing-review, and editing, Sung Kang and Jung-Jae Park: XPS and FIB – FESEM analysis and Kwang-Sun Ryu: Supervision, Conceptualization, Writing-review, and editing.

Competing interests

The authors declare no competing interests.

Additional information

Supplementary information The online version contains supplementary material available at <https://doi.org/10.1038/s43246-024-00514-3>.

Correspondence and requests for materials should be addressed to Kwang-Sun Ryu.

Peer review information *Communications Materials* thanks the anonymous reviewers for their contribution to the peer review of this work. Primary Handling Editors: Jet-Sing Lee. A peer review file is available.

Reprints and permissions information is available at <http://www.nature.com/reprints>

Publisher's note Springer Nature remains neutral with regard to jurisdictional claims in published maps and institutional affiliations.

Open Access This article is licensed under a Creative Commons Attribution 4.0 International License, which permits use, sharing, adaptation, distribution and reproduction in any medium or format, as long as you give appropriate credit to the original author(s) and the source, provide a link to the Creative Commons licence, and indicate if changes were made. The images or other third party material in this article are included in the article's Creative Commons licence, unless indicated otherwise in a credit line to the material. If material is not included in the article's Creative Commons licence and your intended use is not permitted by statutory regulation or exceeds the permitted use, you will need to obtain permission directly from the copyright holder. To view a copy of this licence, visit <http://creativecommons.org/licenses/by/4.0/>.

© The Author(s) 2024